Accurate Estimation of Band Offsets in Group IV Polytype Junctions: a First-principles Study

Thanayut Kaewmaraya, Laetitia Vincent, Michele Amato

To cite this version:

Thanayut Kaewmaraya, Laetitia Vincent, Michele Amato. Accurate Estimation of Band Offsets in Group IV Polytype Junctions: a First-principles Study. Journal of Physical Chemistry C, 2017, 121 (10), pp.5820-5828. ⟨10.1021/acs.jpcc.6b12782⟩. ⟨hal-04453202⟩

Accurate Estimation of Band Offsets in Group IV Polytype Junctions: A First-Principles Study

Thanayut Kaewmaraya,[†,‡] Laetitia Vincent,[‡] and Michele Amato*[,‡]

[†]Department of Physics, Khon Kaen University, Khon Kaen 40002, Thailand

[‡]Centre de Nanosciences et de Nanotechnologies, CNRS, Univ. Paris-Sud, Université Paris-Saclay, C2N - Orsay, 91405 Orsay cedex, France

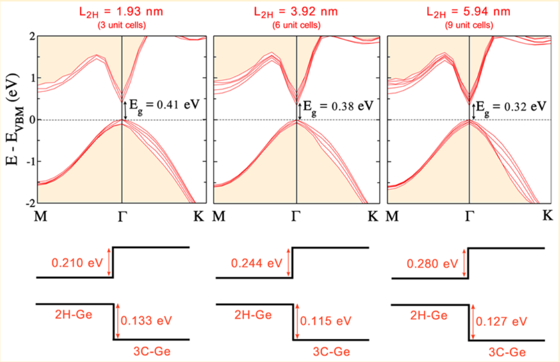

ABSTRACT: Recent advances in the fabrication of group IV homojunctions made by cubic-diamond (3C) and hexagonal-diamond (2H) phases call for a detailed understanding of the physics underlying their electronic structure. In this work, we employ hybrid density functional theory (hybrid-DFT) calculations to study the structural and electronic properties of Si and Ge polytype junctions. Starting from high-resolution transmission electron microscopy (HRTEM) micrographs of 2H/3C Si nanowires, we build a computational model that takes into account both crystal-phase effects and the length of the junction. We obtain accurate estimations of the magnitudes of the band offsets: In particular, we show that 2H/3C Si interfaces induce a type-II band alignment, whereas the Ge structures exhibit a type-I band offset. Furthermore, both Si and Ge homojunctions have direct gaps that are smaller than those of the bulk 3C phase. Finally, we demonstrate that, in all of the considered systems, varying the thickness of the hexagonal phase preserves the nature of the band alignment. Because of the high degree of novelty and the accuracy of the method employed, these results could represent a robust starting point for further experimental investigations in this field.

INTRODUCTION

The crystal structure of Si and Ge nanowires (NWs) at standard conditions usually takes a well-defined cubic-diamond phase, as in the case of their bulk counterparts.[1−4] Nevertheless, the possibility of synthesizing NWs exhibiting other phases, namely, the hexagonal-diamond phase, was recently demonstrated. For example, Hauge et al. obtained pure and stable hexagonal-diamond Si NWs using hexagonal GaP NWs as a template.[5] Other studies have instead succeeded in growing Si and Ge NWs containing both the cubic-diamond and hexagonal-diamond phases, opening the way to the fabrication of well-ordered group IV polytype homojunctions.[6−9] In these materials, the hexagonal-diamond phase appears both as a structural crystal imperfection (i.e., stacking fault)[10−13] and in more extended domains.[8,9] The latter was recently realized by Vincent et al., who proposed a strain-induced phase transformation for the synthesis of Ge NW polytype homojunctions.[8]

The possibility of synthesizing novel phases for Si and Ge might allow for the achievement of a sophisticated control of the materials' properties, as has already been demonstrated in the cases of light emission efficiency,[14,15] band-gap engineering,[16,17] optical absorption,[16,18−20] and thermal transport.[21−23] Indeed, it is well-known that advanced device functionalities, such as modulation doping, electrical insulation, internal field generation, and charge separation, can be induced by bringing together different materials, that is, forming a heterojunction,[24,25] and taking advantage of how the electronic bands of the two materials align. In this context, the study of group IV polytype homojunctions is particularly appealing. One can intuitively expect that hexagonal-diamond/cubic-diamond junctions in NWs will provide novel properties with respect to the single-phase systems because of the intrinsic band offsets developing at the interface. From this point of view, it is worth noting that an accurate knowledge of band alignment plays a crucial role in the engineering of advanced optical and electronic devices (see, for example, refs 26−29) because of the importance of band alignment for electrical transport across the interface and for optical transitions.

A proper description of band offsets in semiconductors requires the correct prediction of band gaps and band positions. Several theoretical studies on group IV hexagonal-diamond/cubic-diamond polytype homojunctions have been conducted, with misleading results sometimes being reported.[30−32] For example, the conclusions in the case of Si still remain contradictory: It was first reported that hexagonal-diamond/cubic-diamond Si superlattices have a type-I band offset,[30,31] whereas it was later argued that the band alignment was of type II.[20,32] This is mainly due to the well-known limitation of conventional density functional theory (DFT) [in which the

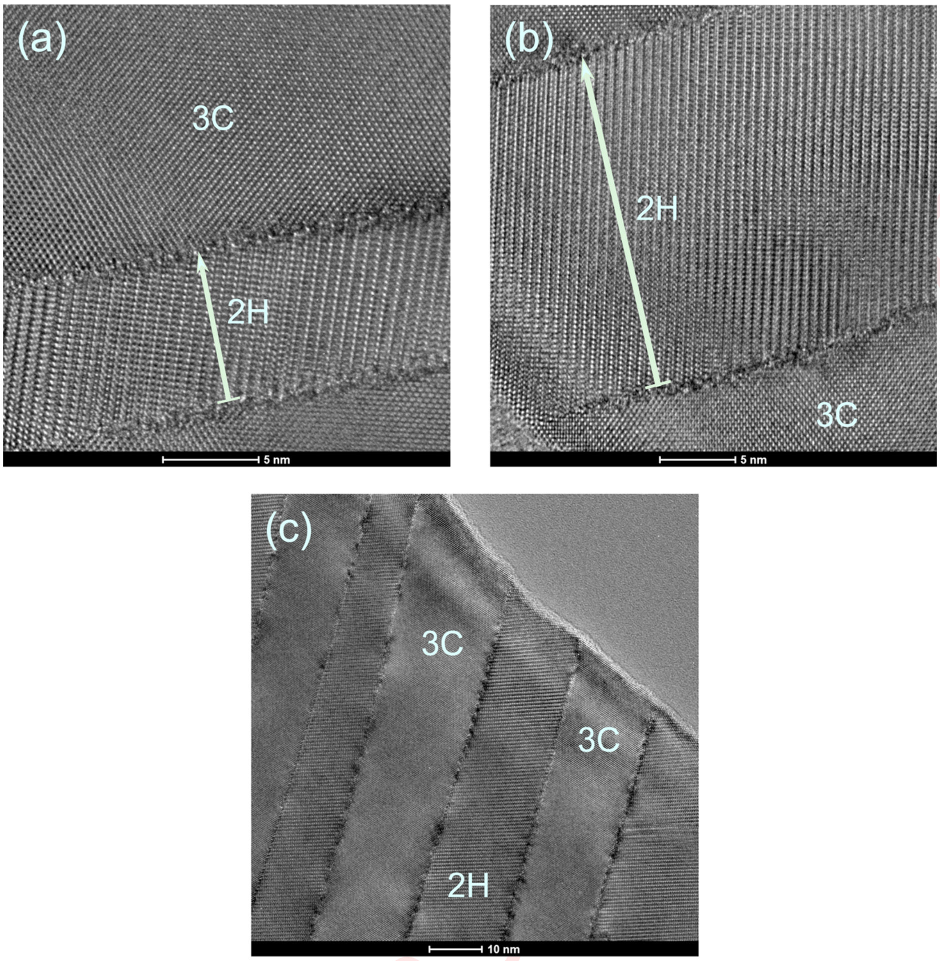

Figure 1. HRTEM micrographs showing the effect of the temperature on the 2H domain size in ⟨111⟩ Si NWs obtained by phase transformation: (a) enlargement of the 2H domain formed at 500 °C, (b) enlargement of the 2H domain formed at 900 °C, and (c) overview of the 2H/3C homojunction obtained at 900 °C. The width of the 2H region and the types of phases are indicated.

exchange-correlation (XC) functionals are derived according to either the local density approximation (LDA) or its gradient-corrected extensions (generalized gradient approximation, GGA)], which severely underestimates band gaps in semiconductors.[33] This limitation is even more pronounced in the case of Ge, for which previous works employing the LDA predicted a metal for both the hexagonal-diamond and cubic-diamond phases, thus making the correct evaluation of valence- and conduction-band discontinuities difficult (see, for example, ref 31).

On the other hand, hybrid density functional theory (hybrid-DFT), which combines Hartree−Fock exchange with conventional DFT, has been demonstrated to be capable of providing precise estimations of band gaps, in particular, in the case of group IV semiconductors.[34−36] Moreover, this method has been successfully employed for the evaluations of band discontinuities of InGaN alloys,[37] two-dimensional semiconducting heterostructures,[38] and polytype rutile−anatase TiO_2.[39,40] Wadehra et al. highlighted the major success of this approach in evaluating the band alignments of numerous technologically important heterostructures.[41] This success is mainly attributed to the inclusion of the Hartree−Fock exact exchange energy in the XC functional, which consequently reduces the self-interaction error.

In this work, we employ hybrid-DFT methods to investigate the structural and electronic properties of group IV hexagonal-diamond/cubic-diamond junctions. Starting from high-resolution transmission electron microscopy (HRTEM) images of 2H/3C Si NWs, we build a computational model that takes into account both crystal-phase effects and the length of the junction. By providing a precise and accurate estimation of band discontinuities, we show that Si junctions induce a type-II band alignment, with the valence-band edge localized on the hexagonal-diamond phase and the conduction-band edge on the cubic-diamond phase. On the other hand, Ge junctions exhibit a type-I band offset, where the valence- and conduction-band edges are both located at the center of the Brillouin zone in the hexagonal-diamond region. Moreover, both Si and Ge homojunctions have direct gaps that are smaller than those of the corresponding bulk cubic-diamond junctions. This might, in principle, be associated with enhanced direct optical transitions. Finally, we demonstrate that, for both Si and Ge junctions, varying the thickness of the hexagonal-diamond phase preserves the nature of the band alignment, as the changes in band discontinuities are negligible.

■ COMPUTATIONAL DETAILS

Structural optimizations and electronic structure calculations were carried out using the VASP code[42] within the framework of DFT. The core−valence interactions were described by a projector-augmented wave (PAW) approach,[43] and four electrons (Si, $3s^23p^2$; Ge, $4s^24p^2$) were treated as the valence states. The exchange-correlation functional was approximated using a hybrid Heyd−Scuseria−Ernzerhof (HSE06) functional.[35] This approach incorporates the error function to screen the slowly decaying Coulomb potential to reduce the computational cost in calculating the Hartree−Fock exact exchange (E_x^{HF}). In more detail, the HSE06 exchange-correlation can be written as

$$E_{xc}^{HSE} = \alpha E_x^{HF,SR}(\mu) + (1 - \alpha)E_x^{PBE,SR}(\mu) + E_x^{PBE,LR}(\mu) + E_c^{PBE} \tag{1}$$

where E_c^{PBE} denotes the Perdew−Burke−Ernzerhof (PBE) correlation functional,[44] α is an empirical mixing value, and μ is an adjustable parameter that decouples the short-range (SR) Coulomb potential from the long-range (LR) counterpart. The standard values of $\alpha = 0.25$ and $\mu = 0.2$ are typically referred to HSE06.[35] This hybrid functional yields good results (such as lattice parameters and band gaps), especially for small- to medium-gap semiconductors (such as Si and Ge) because adding 25% of the HF exchange is the suitable amount for weak dielectric screening.[36] The energy cutoff for representing the plane-wave basis was set to 500 eV. A k-point mesh of $8 \times 8 \times 1$ was used for Brillouin zone sampling of the junctions. Structural optimizations were satisfactorily terminated when the residual Hellmann−Feynman forces exerted on each atom became less than 0.02 eV/Å. Spin−orbit coupling (SOC) effects were considered only in the case of Ge bulk crystals.

We first considered Si and Ge bulk crystal structures. The cubic-diamond phase exhibits the ABC stacking sequence along the ⟨111⟩ direction and, in the Ramsden nomenclature, corresponds to a 3C structure. The same phase can be obtained by considering a hexagonal cell containing six atoms. On the other hand, an ABAB packing pattern along the c direction characterizes the hexagonal-diamond polytype (hence denoted as 2H), which has four atoms in the unit cell. This 2H structure belongs to the space group $P6_3/mmc$ (D_{6h}^4) and exhibits lower symmetry than the cubic-diamond phase, which instead belongs to the space group $Fd\bar{3}m$ (O_h^7). Despite this dissimilarity, the tetrahedral coordination is preserved in both the 3C and 2H phases.

We also considered 2H-[0001]//3C-⟨111⟩ junctions represented by the 72-atom unit cell constructed from the HSE06-relaxed unit cells of 3C and 2H (as shown in Figure 3 below). The lateral lattice constant of the junctions was fixed to that of the 3C phase, meaning that a small amount of intrinsic stress was imposed on the 2H phase. Band structures were determined along the M → Γ → K path according to the hexagonal symmetry. The length of the 72-atom unit cell along the c-axis was large enough (∼12 nm) to make the first Brillouin zone a hexagon.[45]

The proposed structural models were built on the basis of high-resolution transmission electron microscopy (HRTEM) characterization that we performed on 2H/3C-⟨111⟩ Si NW junctions synthesized following the procedure presented in ref 8. In particular, we report in Figure 1 an example of how the sizes of the 2H domains in Si NWs can be tuned by adjusting the temperature of the phase transformation process. At 500 °C (Figure 1a), the 2H Si domains are 7−8 nm in width, whereas at 900 °C (Figure 1b), the width increases to 20 nm. Figure 1c shows an enlarged view of the resulting homojunction at 900 °C. More details about the synthesis and HRTEM characterization are given in ref 46.

Driven by these experimental observations, we decided to study how the variation of the thickness of the hexagonal region influences the electronic properties of the junction. Indeed, as shown in previous studies,[47] the variation of the width of the 2H region in such systems can affect the magnitude of the band offsets. Because of the high computational cost of hybrid-DFT, we could not handle systems with the same size as the experimental samples. Consequently, we restricted our analysis to smaller 2H domains, aiming to elucidate how the properties of the junction can depend on the length of 2H region. We modeled this aspect by considering different junctions obtained by varying the thickness of the 2H phase (denoted by L_{2H} in Figure 3) from three to nine 2H unit cells, but keeping the total length of the junction constant. The considered structures were periodic in all directions of space. This means that our findings are valid for large-diameter NWs (far from the quantum confinement regime) and layered systems.

The structural optimizations of the junctions were performed using the PBE functional, whereas the electronic properties were then evaluated using HSE06. The band offsets in such systems are usually determined by utilizing the average potential method,[48,49] in which the valence- and conduction-band offsets (ΔE_v^{3C-2H} and ΔE_c^{3C-2H}, respectively) are estimated by the expressions

$$\Delta E_v^{3C-2H} = \Delta E_{VBM}^{3C-2H} + \Delta V_{dis}^{3C-2H} \tag{2}$$

$$\Delta E_c^{3C-2H} = \Delta E_g^{3C-2H} + \Delta E_v^{3C-2H} \tag{3}$$

where ΔE_g^{3C-2H} represents the difference between the band gaps of the 3C and 2H phases and ΔE_{VBM}^{3C-2H} is the difference between the valence-band maxima (VBM) of the 3C and 2H bulk phases. The positions of the bulk valence-band edges were measured with respect to the average of the electrostatic potential in each bulk material. On the other hand, ΔV_{dis}^{3C-2H} represents the discontinuity of the average electrostatic potential between the 3C and 2H phases across the interface of the junction. Although this method is very accurate for the determination of band offsets in the limit of an isolated interface, it is not appropriate for the calculation of the band lineups for very thin superlattices or confined systems, as is the case of the junctions in Figure 3a,b. This is mainly due to the rapidly oscillating nature of the electrostatic potential and its small discontinuities in the case of homojunctions that make the determination of an energy reference level difficult. To resolve this issue, in this work, we evaluated the band offset by employing an extensive analysis of the spatial localization of wave functions, as was successfully done in other works.[50,51] This semiquantitative method is based on a careful examination of the spatial distributions of single-particle wave functions in the proximity of valence- and conduction-band edges. Band offsets are then calculated as energy differences between the eigenvalues corresponding to the electronic state of a band edge, which can be localized in a 3C or 2H segment, and the first electronic state, which is completely delocalized (i.e., not confined in a specific region of the junction). The method of the average reference potential was instead used only to further check the results obtained for the junction with $L_{2H} = 5.94$ nm (Figure 3c).

■ RESULTS AND DISCUSSION

Bulk Structures. As an initial step, we performed calculations on bulk crystal structures. The optimized lattice

Table 1. Calculated Lattice Constants of Si and Ge

crystal structure	*a* (Å)	*c* (Å)	*c*/*a* (Å)	*u* (Å)	notes
			Si		
cubic-diamond (3C)	5.435				this work (HSE06)
	5.435				calc[33]
	5.431				expt[54]
hexagonal-diamond (2H)	3.830	6.321	1.650	0.373	this work (HSE06)
	3.828	6.325	1.652	0.374	calc[16]
	3.800	6.269	1.650	0.374	calc[53]
	3.837	6.317	1.646		expt[55]
			Ge		
cubic-diamond (3C)	5.680				this work (HSE06)
	5.682				calc[33]
	5.657				expt[54]
hexagonal-diamond (2H)	4.010	6.590	1.643	0.378	this work (HSE06)
	3.960	6.450	1.629		calc[56]
	3.960	6.570			expt[57]

constants reported in Table 1 show very good agreement with the results of previous studies.[32,52] The *c*/*a* ratios evaluated for both 2H Si and 2H Ge are larger than those for the ideal 2H polytype. This discrepancy is related to the tendency of Si and Ge to normally crystallize in the 3C phase.[32,53]

It is worth noting that the difference in the growth-direction lattice constants of these allotropes is less than 0.5%, indicating that the 2H-[0001]//3C-⟨111⟩ interface is ideally lattice-matched.

Regarding total energies, the 2H phases of both Si and Ge present higher values than the corresponding 3C phases, as already shown in previous LDA studies.[32,53] In particular, the differences in total energy between the 2H and 3C bulk phases amount to 17.3 meV/atom for Si and 14.2 meV/atom for Ge.

The calculated band structures of bulk Si and Ge are presented in Figure 2, and the corresponding band gaps are summarized in Table 2. For the 3C phases, the values obtained by the HSE06 functional are in close agreement with experimental findings.[54]

Interestingly, it is possible to directly compare the electronic band structures of cubic-diamond and hexagonal-diamond crystals by mapping their high-symmetry points in the Brillouin zone (BZ) (for a detailed discussion of the correspondence of the *k*-point groups between the BZs of the 3C and 2H phases, see refs 30 and 58). The cubic-diamond phase contains two basis atoms in the unit cell, whereas there are four atoms in the unit cell of the hexagonal-diamond phase. The later has twice as many bands as the former. Hence, there is a two-to-one correspondence of the high-symmetry points in the irreducible BZ passing from the cubic-diamond phase to the hexagonal-diamond phase. The Γ and L points in the cubic BZ are mapped onto the Γ point in the hexagonal BZ. Both X and L correspond to a point on the line U of the hexagonal-diamond BZ. This is why, for both Si and Ge, the band edges of the 3C and 2H phases occur at different points.

This band-mapping approach can be easily evidenced by examining the band structures of the 3C phase represented in both cubic and hexagonal symmetries, as illustrated in Figure 2a,b for Si and in Figure 2d,e for Ge. The fundamental gaps of the cubic-diamond phase are identical regardless of the symmetrical representation (i.e., 1.14 eV for Si and 0.73 eV for Ge). The valence-band maxima are all located at the Γ-point. In the hexagonal symmetry, the conduction-band edge of Si appears at the point near M located on the line U of the hexagonal BZ, whereas that of Ge occurs at Γ according to the folding from L to Γ. For the 2H phase, in both Si and Ge, the valence- and conduction-band edges occur at the same point as those of the cubic-diamond phases represented in hexagonal symmetry. A reduction of the band gap is also observed for the two semiconductors. Interestingly, 2H Ge is characterized by a direct gap whose value is in fair agreement with recent GW calculations.[56] As demonstrated in previous theoretical works (see, for example, ref 59), in the case of Ge, the inclusion of spin−orbit coupling (SOC) is responsible for a reduction of the fundamental band gap that, in our case, amounts to nearly 0.1 eV for both phases (see the fourth column of Table 2).

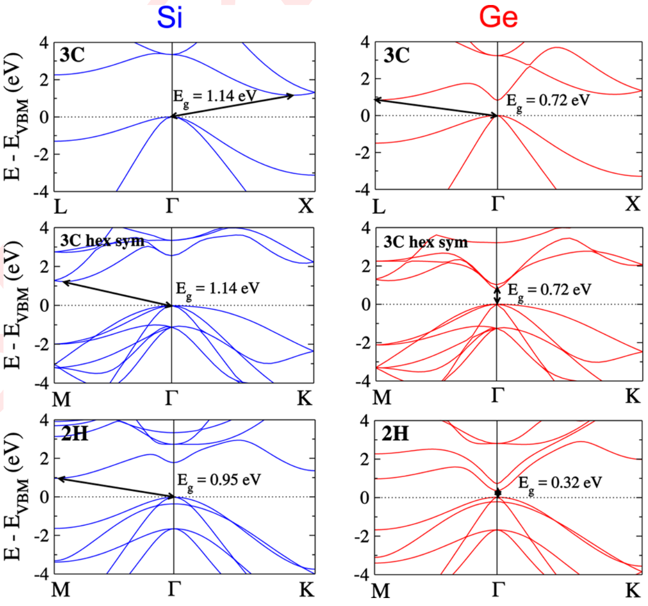

Figure 2. Band structures of bulk (a) cubic-diamond Si, (b) cubic-diamond Si in hexagonal symmetry, (c) hexagonal-diamond Si, (d) cubic-diamond Ge, (e) cubic-diamond Ge in hexagonal symmetry, and (f) hexagonal-diamond Ge. The valence-band maximum (VBM) has been shifted to zero for the sake of visualization.

The universal reduction of the gap of the group IV 2H allotrope with respect to the 3C allotrope is associated with the distinct stacking sequence where structures with higher

Table 2. Calculated Band Gaps of Si and Ge

crystal structure	E_g at Γ (eV)	E_g (eV)	E_g (SOC) (eV)	band edge	notes
			Si		
cubic-diamond (3C)	3.29	1.14		Γ−X	this work (HSE06)
	3.20	1.14		Γ−X	calc[16]
	3.33	1.15		Γ−X	calc[33]
	3.40	1.17		Γ−X	expt[61]
hexagonal-diamond (2H)	1.70	0.95		Γ−M	this work (HSE06)
	1.63	0.95		Γ−M	calc[16]
			Ge		
cubic-diamond (3C)	0.84	0.72	0.61	Γ−L	this work (HSE06)
	0.94	0.85	0.71	Γ−L	calc[33]
	0.81	0.66		Γ−L	expt[54]
hexagonal-diamond (2H)	0.32		0.23		this work (HSE06)
	0.23				calc[56]
	0.31				calc[17]

hexagonality exhibit larger gaps.[31,60] In addition, there is a visible split-off band right below the valence-band maximum (VBM) in the 2H phase. This band originates from the 3-fold-degenerate VBM in the cubic-diamond crystal that splits into a 2-fold Γ_{6v} (p_x and p_y) band and a lower one-fold Γ_{1v} (p_z) band. The splitting energy (E_{cr}) determines the variation of the interactions caused by the change in symmetry.[31] The calculated values of E_{cr} amount to 0.44 eV for Si (in agreement with a recent study employing many-body GW methods[16]) and 0.29 eV for Ge. It is worth mentioning that the gap at Γ of 2H Si is 1.70 eV, remarkably less than that of 3C Si.

Polytype Junctions. After having acquired basic information concerning the bulk phases, we proceeded to a study of the 2H-[0001]//3C-⟨111⟩ polytype junctions. As expected, the geometry relaxation of the junctions (whose atomic structures are shown in Figure 3) revealed that the structural discontinuity and stress at the interface cause only minor atomic rearrangements. This was confirmed by the deviations of the Si−Si and Ge−Ge bond distances and bond angles by less than 0.5% with respect to the corresponding values for the bulk phase.

In terms of the total energies, the junction with three 2H unit cells (L_{2H} = 1.93 nm) is the most stable, and the stability decreases with increasing 2H thickness. For Si, the junctions with six and nine 2H unit cells, corresponding to L_{2H} = 3.92 nm and L_{2H} = 5.94 nm, respectively, exhibit higher energies than that with three 2H unit cells by 0.12 and 0.24 eV/interface, respectively. The same is trus for Ge, with corresponding values of 0.24 and 0.48 eV/interface, respectively. These findings are related to the fact that, for both Si and Ge, the bulk 2H phase is less stable than the bulk 3C phase[62] and, hence, increasing the number of 2H atomic layers induces instability. A related point to consider is that the distance between the periodic images of the 2H regions is at least 60 Å. Thus, the physics of our model does not contain any fictitious interactions between the hexagonal-diamond segments. The modeled junctions correspond to a set of independent quantum wells, and there is no penetration of wave functions between the nearby wells that could yield mini-bands.[63,64] However, a brief word of caution is in order here: The analysis of the stability through total energy arguments does not take into account the effect of the temperature, and it is thus quite far from the complex growth dynamics of such types of systems.

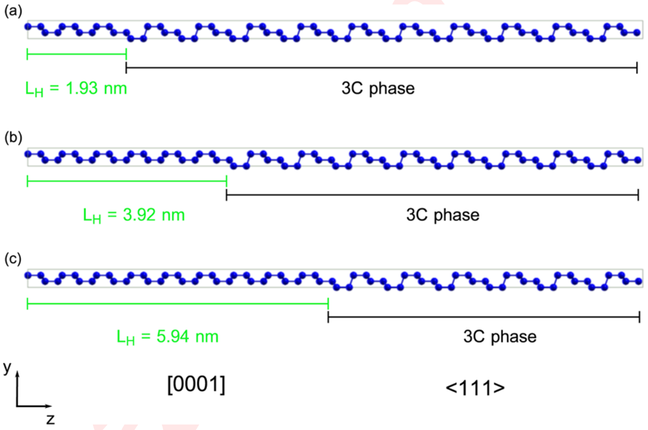

Figure 3. View in the plane (*yz*) of the atomic structures of the 2H-[0001]//3C-⟨111⟩ Si and Ge junctions with 2H regions of different thicknesses: (a) three 2H unit cells (L_{2H} = 1.93 nm), (b) six 2H unit cells (L_{2H} = 3.92 nm), and (c) nine 2H unit cells (L_{2H} = 5.94 nm). All of the junctions contain 72 atoms. The structure are periodic in all of the directions. Blue spheres represent Si or Ge atoms.

To obtain information regarding band offsets, we calculated the projected density of states (PDOS), as shown in Figure 4a. The Si junction containing nine 2H unit cells (L_{2H} = 5.94 nm) induces a staggered band lineup (also known as a type-II band offset). This is clear if one examines the plots of the localization of wave functions corresponding to the band edges (Figure 4b). The wave function of the valence-band edge is completely localized in the 2H region, whereas that of the conduction-band edge appears only in the 3C phase region of space. This behavior is a general characteristic of 2H/3C Si junctions, already observed in 2H-[0001]//3C-⟨111⟩ Si superlattices[32] and, more recently, in thin 2H-[0001]//3C-⟨111⟩ polytype Si nanowires.[20]

On the other hand, the Ge junction with L_{2H} = 5.94 nm exhibits a straddling band lineup (type-I band offset), as one can deduce from the PDOS (Figure 4c) and the spatial localization of the wave functions corresponding to the band edges (Figure 4d).

Remarkably, in spite of having different types of band offsets, for both the Si and Ge junctions, the band gap changes only slightly when the length of the 2H region is reduced from nine to three unit cells (see the insets of Figure 4a,c). This means that the nature and values of the band discontinuities are almost independent of the length of the 2H region.

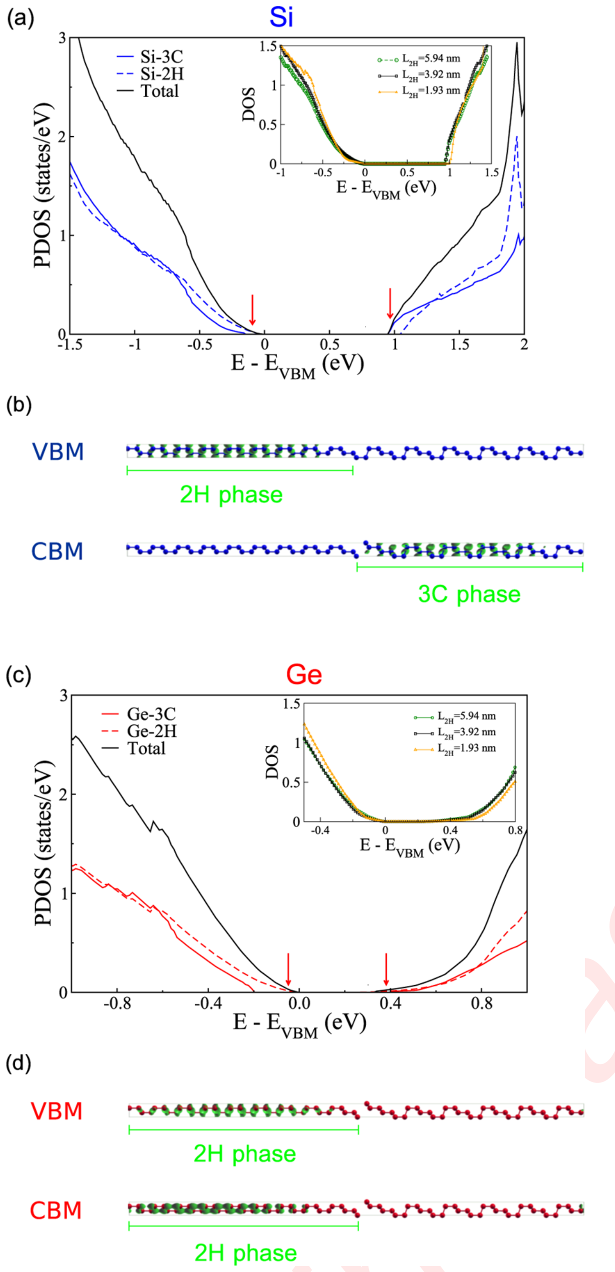

Figure 4. (a,c) Projected densities of states (PDOS) of the 2H-[0001]/3C-⟨111⟩ junctions of (a) Si and (c) Ge containing nine 2H unit cells (L_{2H} = 5.94 nm), indicating that (a) the Si junction induces a staggered band lineup whereas (c) the Ge junction is characterized by a type-I band lineup. (b,d) These findings are also supported by the spatial localization of the wave functions corresponding to band edges for (b) Si and (d) Ge. The total DOS shown in the insets of panels a and c indicate that the variation of L_{2H} from three to nine 2H unit cells yields only a minor change in the band gap. In all of the plots, the valence-band maximum (VBM) has been shifted to zero for the sake of visualization.

We computed the values of the band offsets by analyzing the localization of the wave functions following the method already presented in refs 51 and 65. In the case of the junction with nine 2H unit cells (L_{2H} = 5.94 nm), we further checked our results by also calculating the band lineup with the average potential technique described previously, and we found very good agreement.

Figure 5 shows the band structures of Si junctions (top panel) projected onto the 3C bulk band structure (shaded regions) together with the calculated magnitudes of the band offsets (bottom panel). For the Si junction with L_{2H} = 5.94 nm (right graph), the discontinuities of the valence and conduction bands are 0.123 and 0.094 eV, respectively. These band offsets lead to a finite quantum well. Holes are trapped in the hexagonal region with a relatively deeper well, whereas electrons are confined in cubic region with a shallow barrier. The band gap of the junction is indirect at the point near M because the conduction-band edges of both the 3C and 2H bulk polytypes are located near this point. This staggered band lineup could induce several interesting properties, such as an enhanced photocatalytic activity due to the natural separation of photoexcited charge carriers (as for the case of polytype anatase−rutile TiO_2[39,40] and mixed-phase TiO_2 particles[66−69]).

Varying the 2H thickness (i.e., modifying the length of the 2H region embedded in the 3C phase) preserves the type-II feature as the changes in energy offsets are very small (see the bottom panel of Figure 5). Interestingly, this behavior differs from that observed in our recent work on Si NW polytypes, in which we demonstrated that the band offsets are diameter-dependent, namely, type I at smaller diameter and type II at larger diameters.[20] The dissimilarity is due to the enhanced quantum confinement in thin NWs with respect to the systems considered in this study. We argue that the behavior we report here should be observed in large-diameter NWs.

The difference in the magnitudes of the conduction-band offsets for Si junctions with L_{2H} = 1.93 nm and L_{2H} = 3.92 nm is quite small. This can lead to some difficulty and ambiguity in identifying the band offsets of 2H/3C Si interfaces unless the position of the conduction-band edge in *k*-space is precisely determined.[32] The tiny band offsets in the Si junctions can be ascribed to the fact that the difference in the fundamental gaps of the bulk 2H and 3C phases is nearly 0.2 eV. In addition, increasing the value of L_{2H} gives rise to more discretized bound states of the 2-fold Γ_{6v} band (p_x and p_y) of 2H phase near the valence-band edge. The energy spacings between them are large for L_{2H} = 1.93 nm (i.e., the narrow well), and they gradually become narrower as this parameter is increased. This is basically a consequence of the particle-in-a-box model, where the increase in the number of discretized states for thicker 2H regions comes from the increasing number of particles (i.e., holes) being confined in the quantum well. The 2-fold Γ_{6v} feature remains unaltered, indicating that the degeneracy of the holes is not influenced by the quantum confinement. The numbers of bound states in the valence bands of 2H inclusions with L_{2H} = 3.92 nm and L_{2H} = 5.94 nm are similar. On the other hand, this behavior is not observed for the conduction-band offsets where electrons are trapped. This is because the offset is so small that electrons are not strongly confined.

Unlike Si junctions, Ge junctions composed of nine 2H unit cells are characterized by a type-I band lineup with a direct band gap of 0.32 eV as depicted in Figure 6 (right graph). The top of the valence band and the bottom of the conduction band are located at the Γ-point of the 2H region, meaning that the band-gap transition is direct not only in *k*-space but also in real space. The valence- and conduction-band offsets amount to 0.127 and 0.280 eV, respectively. Therefore, both electrons and holes are confined in 2H Ge regions, but electrons are trapped more strongly than holes. Notably, the magnitudes of the conduction-band discontinuities in Ge junctions are relatively greater than those in Si junctions. This is probably due to the

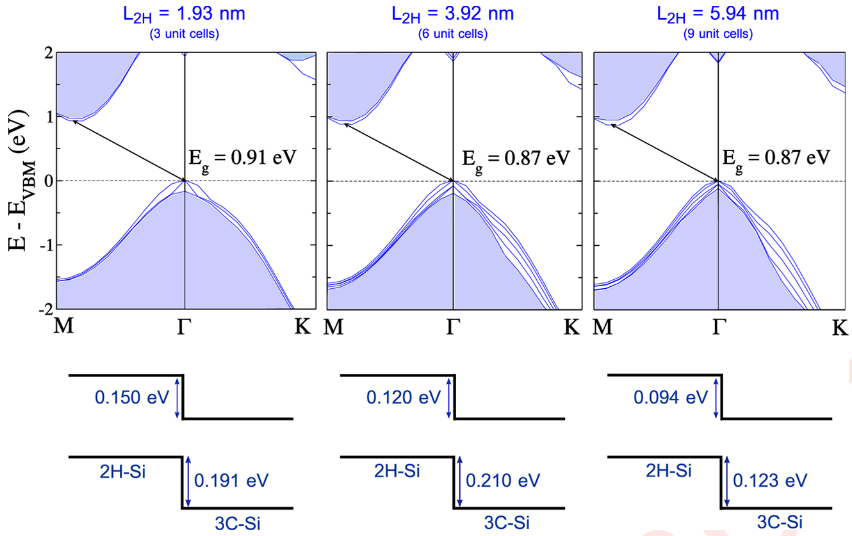

Figure 5. Band structures of Si junctions as a function of the thickness of the hexagonal-diamond region, denoted by L_{2H} for three different cases: L_{2H} = 1.93 nm (left), L_{2H} = 3.92 nm (center), and L_{2H} = 5.94 nm (right). The band structures of the junctions are projected onto the 3C bulk band structure (shaded regions). The valence-band maximum (VBM) has been shifted to zero for the sake of visualization. The schematic band lineup (not to scale) is illustrated below each band structure.

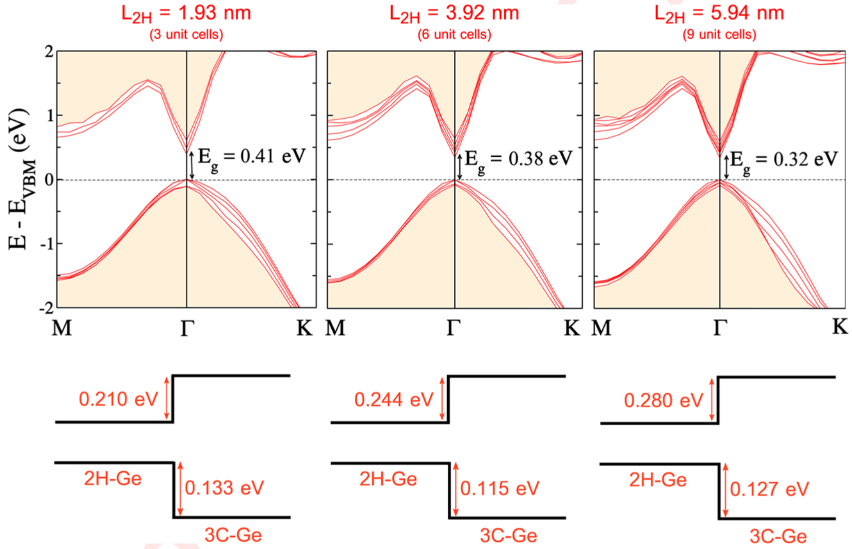

Figure 6. Band structures of Ge junctions as a function of the thickness of the hexagonal-diamond region, denoted by L_{2H} for three different cases: L_{2H} = 1.93 nm (left), L_{2H} = 3.92 nm (center), and L_{2H} = 5.94 nm (right). The band structures of the junctions are projected onto the 3C bulk band structure (shaded regions). The valence-band maximum (VBM) has been shifted to zero for the sake of visualization. The schematic band lineup (not to scale) is illustrated below each band structure.

fact that the fundamental band gap of bulk 3C Ge (0.72 eV) differs considerably from that of 2H Ge (0.32 eV) and that quantum confinement in Ge is more pronounced than that in Si.

As in the case of Si, variation of the thickness of the 2H region in Ge junctions does not create a significant change in the band gap, type, or magnitude of the band offsets, as shown in Figure 6 (bottom panel). The junctions with L_{2H} = 1.93 nm and L_{2H} = 3.92 nm maintain a semiconducting character, with band gaps of 0.41 and 0.38 eV, respectively. The band lineup remains of type I for all of the cases, and the magnitude of the energy offsets deviates slightly from that of the junction containing nine 2H unit cells. Even here, we observed the presence of discretized bound states at the valence- and conduction-band edges as a consequence of quantum confinement. The energy spacings decreases with increasing thickness of the hexagonal phase. Notably, the degeneracy of the 2-fold Γ_{6v} (p_x and p_y) feature of the 2H phase in the valence band was further shifted when L_{2H} was reduced to 1.93 nm. On the other hand, this circumstance does not occur in junctions with thicker hexagonal segments where such degeneracy is still maintained.

■ CONCLUSIONS

We employed hybrid density functional theory (hybrid-DFT) calculations to investigate the structural and electronic properties of 2H/3C group IV homojunctions. We found that Si junctions are characterized by a type-II band alignment, with the valence-band edge localized on the hexagonal-diamond phase and the conduction-band edge localized on the cubic-diamond phase. As already demonstrated in the case of Si NWs, this band lineup could be of some benefit for photovoltaics as well as other advanced technological applications.

On the other hand, Ge junctions exhibit a type-I band lineup where the valence- and the conduction-band edges are both located in the 2H region. This type of band alignment could in principle offer an enhancement in optical transitions as already proposed in the case of Ge superlattices.[70] Yet, our findings indicate that Ge polytype homojunctions present a direct band gap whose value is smaller if compared with the bulk 3C phase one. This property could be related to enhanced direct optical transitions that may be exploited in infrared optoelectronics.

Finally, we have also demonstrated that, for both Si and Ge homojunctions, varying the thickness of the 2H region leaves the nature of the band alignment, the band-gap values, and the offset magnitudes almost unaltered. This indicates that the presence of even short hexagonal segments can give rise to major changes in the properties of the entire crystal (as in the case of 2H regions locally induced by crystal defects).

In view of the recent successful achievements in fabricating Si and Ge polytype NWs,[5,8] all of these findings could guide and help further experimental investigations in this field.

■ AUTHOR INFORMATION

Corresponding Author

*E-mail: michele.amato@u-psud.fr.

ORCID

Michele Amato: 0000-0002-3690-3194

Notes

The authors declare no competing financial interest.

■ ACKNOWLEDGMENTS

We acknowledge support from the Nanodesign project Nanoharvesting funded by the IDEX Paris-Saclay (ANR-11-IDEX-0003-02). The high-performance computing (HPC) resources for this project were granted by the Institut du developpement et des ressources en informatique scientifique (IDRIS) under allocations i2015097422 and i2016097531 through GENCI (Grand Equipement National de Calcul Intensif).

■ REFERENCES

(1) Lu, W.; Lieber, C. M. Semiconductor Nanowires. *J. Phys. D: Appl. Phys.* **2006**, *39*, R387.

(2) Amato, M.; Rurali, R. Surface Physics of Semiconducting Nanowires. *Prog. Surf. Sci.* **2016**, *91*, 1−28.

(3) Amato, M.; Palummo, M.; Rurali, R.; Ossicini, S. Silicon−Germanium Nanowires: Chemistry and Physics in Play, from Basic Principles to Advanced Applications. *Chem. Rev.* **2014**, *114*, 1371−1412.

(4) Rurali, R. Colloquium: Structural, Electronic, and Transport Properties of Silicon Nanowires. *Rev. Mod. Phys.* **2010**, *82*, 427.

(5) Hauge, H. I. T.; Verheijen, M. A.; Conesa-Boj, S.; Etzelstorfer, T.; Watzinger, M.; Kriegner, D.; Zardo, I.; Fasolato, C.; Capitani, F.; Postorino, P.; Kölling, S.; Li, A.; Assali, S.; Stangl, J.; Bakkers, E. P. A. M. Hexagonal Silicon Realized. *Nano Lett.* **2015**, *15*, 5855−5860.

(6) Jeon, N.; Dayeh, S. A.; Lauhon, L. J. Origin of Polytype Formation in VLS-Grown Ge Nanowires through Defect Generation and Nanowire Kinking. *Nano Lett.* **2013**, *13*, 3947−3952.

(7) Biswas, S.; Doherty, J.; Majumdar, D.; Ghoshal, T.; Rahme, K.; Conroy, M.; Singha, A.; Morris, M. A.; Holmes, J. D. Diameter-Controlled Germanium Nanowires with Lamellar Twinning and Polytypes. *Chem. Mater.* **2015**, *27*, 3408−3416.

(8) Vincent, L.; Patriarche, G.; Hallais, G.; Renard, C.; Gardès, C.; Troadec, D.; Bouchier, D. Novel Heterostructured Ge Nanowires Based on Polytype Transformation. *Nano Lett.* **2014**, *14*, 4828−4836.

(9) Qiu, Y.; Bender, H.; Richard, O.; Kim, M.-S.; Van Besien, E.; Vos, I.; de Potter de ten Broeck, M.; Mocuta, D.; Vandervorst, W. Epitaxial Diamond-Hexagonal Silicon Nano-Ribbon Growth on (001) Silicon. *Sci. Rep.* **2015**, *5*, 12692.

(10) Jeon, N.; Dayeh, S. A.; Lauhon, L. J. Origin of Polytype Formation in VLS-Grown Ge Nanowires through Defect Generation and Nanowire Kinking. *Nano Lett.* **2013**, *13*, 3947−3952.

(11) Shin, N.; Chi, M.; Howe, J. Y.; Filler, M. A. Rational Defect Introduction in Silicon Nanowires. *Nano Lett.* **2013**, *13*, 1928−1933.

(12) Lopez, F. J.; Givan, U.; Connell, J. G.; Lauhon, L. J. Silicon Nanowire Polytypes: Identification by Raman Spectroscopy, Generation Mechanism, and Misfit Strain in Homostructures. *ACS Nano* **2011**, *5*, 8958−8966.

(13) Shin, N.; Chi, M.; Filler, M. A. Sidewall Morphology-Dependent Formation of Multiple Twins in Si Nanowires. *ACS Nano* **2013**, *7*, 8206−8213.

(14) Fabbri, F.; Rotunno, E.; Lazzarini, L.; Fukata, N.; Salviati, G. Visible and Infra-red Light Emission in Boron-Doped Wurtzite Silicon Nanowires. *Sci. Rep.* **2014**, *4*, 3603.

(15) Li, Y.; Liu, Z.; Lu, X.; Su, Z.; Wang, Y.; Liu, R.; Wang, D.; Jian, J.; Lee, J. H.; Wang, H.; Yu, Q.; Bao, J. Broadband Infrared Photoluminescence in Silicon Nanowires with High Density Stacking Faults. *Nanoscale* **2015**, *7*, 1601−1605.

(16) Rödl, C.; Sander, T.; Bechstedt, F.; Vidal, J.; Olsson, P.; Laribi, S.; Guillemoles, J.-F. Wurtzite Silicon as a Potential Absorber in Photovoltaics: Tailoring the Optical Absorption by Applying Strain. *Phys. Rev. B: Condens. Matter Mater. Phys.* **2015**, *92*, 045207.

(17) De, A.; Pryor, C. E. Electronic Structure and Optical Properties of Si, Ge and Diamond in the Lonsdaleite Phase. *J. Phys.: Condens. Matter* **2014**, *26*, 045801.

(18) Haberl, B.; Strobel, T. A.; Bradby, J. E. Pathways to Exotic Metastable Silicon Allotropes. *Appl. Phys. Rev.* **2016**, *3*, 040808.

(19) Beekman, M.; Wei, K.; Nolas, G. S. Clathrates and Beyond: Low-Density Allotropy in Crystalline Silicon. *Appl. Phys. Rev.* **2016**, *3*, 040804.

(20) Amato, M.; Kaewmaraya, T.; Zobelli, A.; Palummo, M.; Rurali, R. Crystal Phase Effects in Si Nanowire Polytypes and Their Homojunctions. *Nano Lett.* **2016**, *16*, 5694−5700.

(21) Majumdar, D.; Biswas, S.; Ghoshal, T.; Holmes, J. D.; Singha, A. Probing Thermal Flux in Twinned Ge Nanowires through Raman Spectroscopy. *ACS Appl. Mater. Interfaces* **2015**, *7*, 24679−24685.

(22) Porter, A.; Tran, C.; Sansoz, F. Intrinsic Nanotwin Effect on Thermal Boundary Conductance in Bulk and Single-Nanowire Twinning Superlattices. *Phys. Rev. B: Condens. Matter Mater. Phys.* **2016**, *93*, 195431.

(23) Zhan, H.; Zhang, Y.; Bell, J. M.; Gu, Y. Thermal Conductivity of Si Nanowires with Faulted Stacking Layers. *J. Phys. D: Appl. Phys.* **2014**, *47*, 015303.

(24) Alferov, Z. I. The History and Future of Semiconductor Heterostructures. *Semiconductors* **1998**, *32*, 1−14.

(25) Lauhon, L.; Gudiksen, M. S.; Lieber, C. M. Semiconductor Nanowire Heterostructures. *Philos. Trans. R. Soc., A* **2004**, *362*, 1247−1260.

(26) Chuang, C.-H. M.; Brown, P. R.; Bulović, V.; Bawendi, M. G. Improved Performance and Stability in Quantum Dot Solar Cells through Band Alignment Engineering. *Nat. Mater.* **2014**, *13*, 796.

(27) Robertson, J. Band Offsets of Wide-band-gap Oxides and Implications for Future Electronic Devices. *J. Vac. Sci. Technol., B: Microelectron. Process. Phenom.* **2000**, *18*, 1785−1791.

(28) Kroemer, H. Nobel Lecture: Quasielectric Fields and Band offsets: Teaching Electrons New Tricks. *Rev. Mod. Phys.* **2001**, *73*, 783.

(29) Kang, J.; Tongay, S.; Zhou, J.; Li, J.; Wu, J. Band Offsets and Heterostructures of Two-dimensional Semiconductors. *Appl. Phys. Lett.* **2013**, *102*, 012111.

(30) Murayama, M.; Nakayama, T. Chemical Trend of Band offsets at Wurtzite/zinc-blende Heterocrystalline Semiconductor Interfaces. *Phys. Rev. B: Condens. Matter Mater. Phys.* **1994**, *49*, 4710−4724.

(31) Raffy, C.; Furthmüller, J.; Bechstedt, F. Properties of Hexagonal Polytypes of Group-IV Elements from First-principles Calculations. *Phys. Rev. B: Condens. Matter Mater. Phys.* **2002**, *66*, 075201.

(32) Raffy, C.; Furthmüller, J.; Wagner, J.-M.; Bechstedt, F. *Ab initio* Study of Structural and Electronic Properties of Planar Defects in Si and SiC. *Phys. Rev. B: Condens. Matter Mater. Phys.* **2004**, *70*, 195344.

(33) Hummer, K.; Harl, J.; Kresse, G. Heyd-Scuseria-Ernzerhof Hybrid Functional for Calculating the Lattice Dynamics of Semiconductors. *Phys. Rev. B: Condens. Matter Mater. Phys.* **2009**, *80*, 115205.

(34) Garza, A. J.; Scuseria, G. E. Predicting Band Gaps with Hybrid Density Functionals. *J. Phys. Chem. Lett.* **2016**, *7*, 4165−4170.

(35) Heyd, J.; Scuseria, G. E.; Ernzerhof, M. Hybrid Functionals based on a Screened Coulomb Potential. *J. Chem. Phys.* **2003**, *118*, 8207.

(36) Paier, J.; Marsman, M.; Hummer, K.; Kresse, G.; Gerber, I.; Angyan, J. G. Screened Hybrid Density Functionals Applied to Solids. *J. Chem. Phys.* **2006**, *124*, 154709.

(37) Moses, P. G.; Van de Walle, C. G. Band Bowing and Band Alignment in InGaN Alloys. *Appl. Phys. Lett.* **2010**, *96*, 021908.

(38) Kang, J.; Tongay, S.; Zhou, J.; Li, J.; Wu, J. Band Offsets and Heterostructures of Two-dimensional Semiconductors. *Appl. Phys. Lett.* **2013**, *102*, 012111.

(39) Pfeifer, V.; Erhart, P.; Li, S.; Rachut, K.; Morasch, J.; Brötz, J.; Reckers, P.; Mayer, T.; Rühle, S.; Zaban, A.; Mora Seró, I.; Bisquert, J.; Jaegermann, W.; Klein, A. Energy Band Alignment between Anatase and Rutile TiO_2. *J. Phys. Chem. Lett.* **2013**, *4*, 4182−4187.

(40) Scanlon, D. O.; Dunnill, C. W.; Buckeridge, J.; Shevlin, S. A.; Logsdail, A. J.; Woodley, S. M.; Catlow, C. R. A.; Powell, M. J.; Palgrave, R. G.; Parkin, I. P.; Watson, G. W.; Keal, T. W.; Sherwood, P.; Walsh, A.; Sokol, A. A. Band Alignment of Rutile and Anatase TiO_2. *Nat. Mater.* **2013**, *12*, 798−801.

(41) Wadehra, A.; Nicklas, J. W.; Wilkins, J. W. Band Offsets of Semiconductor Heterostructures: A hybrid Density Functional Study. *Appl. Phys. Lett.* **2010**, *97*, 092119.

(42) Hafner, J. *Ab-initio* Simulations of Materials using VASP: Density-functional Theory and beyond. *J. Comput. Chem.* **2008**, *29*, 2044−2078.

(43) Blochl, P. E. Projector Augmented-wave Method. *Phys. Rev. B: Condens. Matter Mater. Phys.* **1994**, *50*, 17953−17978.

(44) Perdew, J. P.; Burke, K.; Ernzerhof, M. Generalized Gradient Approximation Made Simple. *Phys. Rev. Lett.* **1996**, *77*, 3865−3868.

(45) Iwata, H. P.; Lindefelt, U.; Öberg, S.; Briddon, P. R. Effective Masses of Two-Dimensional Electron Gases around Cubic Inclusions in Hexagonal Silicon Carbide. *Phys. Rev. B: Condens. Matter Mater. Phys.* **2003**, *68*, 245309.

(46) The NWs shown in Figure 1 were obtained by dry etching using a top-down approach. It is worth noting that the phase transformation that we used was demonstrated in ⟨111⟩ Ge and Si NWs grown by a vapor−liquid−solid (VLS) growth process or by top-down etching. The phase transformation was achieved following the procedure described previously.[8] The NWs were embedded in a hydrogen silsesquioxane (HSQ) resist and cured at 500 and 900 °C, with a rapid thermal annealing process for 10 min. The HSQ was then removed with dilute hydrofluoridric acid, and the NWs were dispersed on a carbon TEM membrane. TEM observations were performed using an E-TEM Cs-corrected TITAN FEI instrument operating at 300 keV.

(47) Bechstedt, F.; Käckell, P. Heterocrystalline Structures: New Types of Superlattices? *Phys. Rev. Lett.* **1995**, *75*, 2180−2183.

(48) Baldereschi, A.; Baroni, S.; Resta, R. Band Offsets in Lattice-Matched Heterojunctions: A Model and First-Principles Calculations for GaAs/AlAs. *Phys. Rev. Lett.* **1988**, *61*, 734−737.

(49) Colombo, L.; Resta, R.; Baroni, S. Valence-band Offsets at Strained Si/Ge Interfaces. *Phys. Rev. B: Condens. Matter Mater. Phys.* **1991**, *44*, 5572.

(50) Nduwimana, A.; Musin, R.; Smith, A.; Wang, X.-Q. Spatial Carrier Confinement in Core-shell and Multishell Nanowire Heterostructures. *Nano Lett.* **2008**, *8*, 3341−3344.

(51) Amato, M.; Ossicini, S.; Rurali, R. Band-offset Driven Efficiency of the Doping of SiGe Core−Shell nanowires. *Nano Lett.* **2011**, *11*, 594−598.

(52) Joannopoulos, J. D.; Cohen, M. L. Electronic Properties of Complex Crystalline and Amorphous Phases of Ge and Si. II. Band Structure and Optical Properties. *Phys. Rev. B* **1973**, *8*, 2733−2755.

(53) Yeh, C.-Y.; Lu, Z.; Froyen, S.; Zunger, A. Zinc-blende−Wurtzite Polytypism in Semiconductors. *Phys. Rev. B: Condens. Matter Mater. Phys.* **1992**, *46*, 10086.

(54) Kittel, C. *Introduction to Solid State Physics*, 6th ed.; Wiley: New York, 1986.

(55) Besson, J. M.; Mokhtari, E. H.; Gonzalez, J.; Weill, G. Electrical Properties of Semimetallic Silicon III and Semiconductive Silicon IV at Ambient Pressure. *Phys. Rev. Lett.* **1987**, *59*, 473−476.

(56) Chen, P.-S.; Fan, S.-T.; Lan, H.-S.; Liu, C. W. Band Calculation of Lonsdaleite Ge. *J. Phys. D: Appl. Phys.* **2017**, *50*, 015107.

(57) Xiao, S.-Q.; Pirouz, P. On Diamond-hexagonal Germanium. *J. Mater. Res.* **1992**, *7*, 1406−1412.

(58) Salehpour, M. R.; Satpathy, S. Comparison of Electron Bands of Hexagonal and Cubic Diamond. *Phys. Rev. B: Condens. Matter Mater. Phys.* **1990**, *41*, 3048−3052.

(59) Laubscher, M.; Küfner, S.; Kroll, P.; Bechstedt, F. Amorphous Ge Quantum Dots Embedded in Crystalline Si: Ab initio Results. *J. Phys.: Condens. Matter* **2015**, *27*, 405302.

(60) Kiefer, F.; Hlukhyy, V.; Karttunen, A. J.; Fassler, T. F.; Gold, C.; Scheidt, E.-W.; Scherer, W.; Nylen, J.; Haussermann, U. Synthesis, Structure, and Electronic Properties of 4H-germanium. *J. Mater. Chem.* **2010**, *20*, 1780−1786.

(61) Zucca, R. R. L.; Shen, Y. R. Wavelength-Modulation Spectra of Some Semiconductors. *Phys. Rev. B* **1970**, *1*, 2668−2676.

(62) Mujica, A.; Rubio, A.; Muñoz, A.; Needs, R. J. High-pressure Phases of Group-IV, III˘ V, and II˘ VI Compounds. *Rev. Mod. Phys.* **2003**, *75*, 863−912.

(63) Miller, D. A. B. Optical Physics of Quantum Wells. In *Quantum Dynamics of Simple Systems*; Oppo, G.-L., Barnett, S. M., Riis, E., Wilkinson, M., Eds.; Institute of Physics: London, 1996; pp 239−26.

(64) Weisbuch, C. Fundamental Properties of III−V Semiconductor Two-Dimensional Quantized Structures: The Basis for Optical and Electronic Device Applications. In *Applications of Multiquantum Wells, Selective Doping, and Superlattices*; Dingle, R., Ed.; Semiconductors and Semimetals; Elsevier, 1987; Vol. *24*, Chapter 1, pp 1−133.

(65) Amato, M.; Palummo, M.; Ossicini, S. Segregation, Quantum Confinement Effect and Band Offset for [110] SiGe NWs. *Phys. Status Solidi B* **2010**, *247*, 2096−2101.

(66) Bickley, R. I.; Gonzalez-Carreno, T.; Lees, J. S.; Palmisano, L.; Tilley, R. J. A Structural Investigation of Titanium Dioxide Photocatalysts. *J. Solid State Chem.* **1991**, *92*, 178−190.

(67) Hurum, D. C.; Agrios, A. G.; Gray, K. A.; Rajh, T.; Thurnauer, M. C. Explaining the Enhanced Photocatalytic Activity of Degussa P25 Mixed-Phase TiO2 Using EPR. *J. Phys. Chem. B* **2003**, *107*, 4545−4549.

(68) Ohno, T.; Sarukawa, K.; Tokieda, K.; Matsumura, M. Morphology of a TiO2 Photocatalyst (Degussa, P-25) Consisting of Anatase and Rutile Crystalline Phases. *J. Catal.* **2001**, *203*, 82−86.

(69) Kho, Y. K.; Iwase, A.; Teoh, W. Y.; Mädler, L.; Kudo, A.; Amal, R. Photocatalytic H2 Evolution over TiO2 Nanoparticles. The Synergistic Effect of Anatase and Rutile. *J. Phys. Chem. C* **2010**, *114*, 2821−2829.

(70) Ikonic, Z.; Srivastava, G. P.; Inkson, J. C. Direct Optical Transitions in Indirect Semiconductors: The case of Ge Twinning Superlattices. *Phys. Rev. B: Condens. Matter Mater. Phys.* **1995**, *52*, 1474−1476.